

1 **Full-field modeling of heat transfer in asteroid regolith 2: Effects of porosity**

2

3 Andrew J. Ryan¹, Daniel Pino-Muñoz², Marc Bernacki², Marco Delbo³, Naoya Sakatani⁴, Jens
4 Biele⁵, Joshua P. Emery⁶, Benjamin Rozitis⁷

5

6 ¹Lunar and Planetary Laboratory, University of Arizona, Tucson, AZ, USA.

7 ²Centre de mise en forme des matériaux (CEMEF), Mines ParisTech, PSL Research University,
8 Sophia Antipolis, France.

9 ³Observatoire de la Côte d'Azur, CNRS-Lagrange, Université Côte d'Azur, Nice, France.

10 ⁴Rikkyo University, Tokyo, Japan.

11 ⁵German Aerospace Center (DLR), Köln, Germany.

12 ⁶Department of Astronomy and Planetary Sciences, Northern Arizona University, Flagstaff, AZ,
13 USA.

14 ⁷School of Physical Sciences, The Open University, Milton Keynes, UK.

15

16 Corresponding author: Andrew Ryan (ajryan4@arizona.edu)

17

18 **Key Points:**

- 19 • A 3D finite element model is used to study the effects of regolith porosity and material
20 properties on the radiative thermal conductivity.
- 21 • A new, empirical model for regolith radiative thermal conductivity is presented.
- 22 • We show that regolith packing density has a minimal effect on predicted regolith particle
23 sizes from thermal inertia on airless bodies.

24 **Abstract**

25 The thermal conductivity of granular planetary regolith is strongly dependent on the porosity, or
26 packing density, of the regolith particles. However, existing models for regolith thermal
27 conductivity predict different dependencies on porosity. Here, we use a full-field model of
28 planetary regolith to study the relationship between regolith radiative thermal conductivity,
29 porosity, and the particle non-isothermality. The model approximates regolith as regular and
30 random packings of spherical particles in a 3D finite element mesh framework. Our model
31 results, which are in good agreement with previous numerical and experimental datasets, show
32 that random packings have a consistently higher radiative thermal conductivity than ordered
33 packings. From our random packing results, we present a new empirical model relating regolith
34 thermal conductivity, porosity, temperature, particle size, and the thermal conductivity of
35 individual particles. This model shows that regolith particle size predictions from thermal inertia
36 are largely independent of assumptions of regolith porosity, except for when the non-
37 isothermality effect is large, as is the case when the regolith is particularly coarse and/or is
38 composed of low thermal conductivity material.

39

40 **Plain language summary**

41 The temperature of a planetary surface is strongly controlled by the thermal inertia of the surface
42 materials. Specifically, if the surface is covered in a granular regolith, then the size, thermal
43 conductivity, and packing density of the regolith particles strongly affects the surface thermal
44 inertia, which in turn controls surface temperatures. In this work, we use 3D numerical
45 simulations of heat transfer through beds of spherical particles, representing a planetary regolith,
46 to investigate how thermal conductivity and thermal inertia are controlled by the packing density
47 and thermal conductivity of the spheres. Our results are presented in the form of a new empirical
48 model, which could be used to calculate regolith thermal conductivity from knowledge of
49 particle size, composition, and packing density. The use of this model is demonstrated in the
50 typical reverse fashion, where an observed planetary thermal inertia is converted into a predicted
51 regolith particle size. Our model shows that the predicted particle size is largely independent of
52 regolith particle packing density, in contrast to other common regolith models.

53

54 **1 Introduction**

55 The thermal conductivity of planetary regolith can be estimated from remote surface
56 temperature observations using a planetary thermophysical model (e.g., Delbo et al., 2015; Grott
57 et al., 2019; Rozitis et al., 2020). The thermal conductivity of a regolith in vacuum is sensitive to
58 many physical properties of the regolith, such as particle size, porosity (or packing density), and
59 the material properties of the individual particles (e.g., emissivity and thermal conductivity;
60 Wechsler et al., 1972; Kaviany, 1995). Thus, remote estimates of regolith thermal conductivity
61 allow for study of geologic processes that affect the regolith, such as meteoroid bombardment,
62 thermal fracturing, and mass wasting (Cambioni et al., 2021). Robotic and crewed missions
63 furthermore often rely on a constrained knowledge of regolith properties to ensure the success of
64 mission objectives, such as sampling and landing (e.g., Ferguson et al., 2006; Emery et al.,
65 2014).

66 In this work, we build upon developments from a previous paper (Ryan et al., 2020) to
67 develop an advanced understanding of the relationship between regolith radiative thermal
68 conductivity, porosity, and material properties. We again utilize a 3D finite element mesh
69 framework where regolith is approximated as ordered and random packings of spherical
70 particles, with the added improvement of periodicity to limit model edge effects. We find a new
71 empirical fit between the radiative exchange factor, used to calculate radiative thermal
72 conductivity, porosity, and regolith particle thermal conductivity and temperature. Our results
73 compare well to experimental datasets and to more limited numerical model results from other
74 researchers. Throughout this work, we use the word “porosity” to denote the relative fraction of
75 void space between regolith particles, otherwise known as macroporosity or the inverse of
76 particle bed packing density. This is not to be confused with microporosity, which is the pore
77 space within an individual regolith particle.

78

79 **2 Background**

80 There are two relevant modes of heat transfer between opaque particles in vacuum —
81 radiation between particle surfaces and conduction across the contacts between particles
82 (Wesselink, 1948; Watson, 1964; Wechsler et al., 1972; van Antwerpen et al., 2010). These two
83 heat transfer mechanisms are typically represented in terms of their effective thermal
84 conductivity, where thermal conductivity due to radiative heat transfer is denoted by k_r and
85 thermal conductivity due to the contacts between the particles, referred to herein as “solid
86 conductivity,” is denoted by k_s . The total thermal conductivity of the regolith particulate
87 assemblage may thus be expressed as $k = k_s + k_r$.

88 In a previous study, we focused our efforts on examining how bulk radiative thermal
89 conductivity, k_r , of a regolith is related to particle size frequency distribution and material
90 properties (Ryan et al., 2020). In this present work, we again focus on investigating the radiative
91 thermal conductivity of regolith for two reasons. First, radiative thermal conductivity on airless
92 bodies is typically much larger than the conductivity due to particle-to-particle contacts in coarse
93 particulate regoliths (i.e., $> \sim 5$ mm, Ryan et al., 2020, Sakatani et al., 2017; Gundlach and Blum,
94 2013), which are of high interest for recent missions to rubble-pile asteroids (OSIRIS-REx and
95 Hayabusa2) that have regolith that is likely coarse, where present (Rozitis et al., 2020; Cambioni
96 et al., 2021).

97 The second reason for focusing on radiative conductivity is that it is much less well
98 constrained as a function of regolith porosity than is conductivity due to contacts; different
99 models predict distinctive trends of k_r versus porosity. For example, with a doubling in porosity
100 from 0.4 to 0.8, the models by Sakatani et al. (2017) and Gundlach and Blum (2013) predict
101 increases in k_r that differ by a factor of ~ 6 . The value of k_s , conversely, is less variable between
102 models and instead depends on the accuracy of the correlation that is used to relate coordination
103 number (i.e., the mean number of contact points per particle) to porosity and assumptions of
104 particle-to-particle cohesion and contact deformation (e.g., Sakatani et al., 2017; Arakawa et al.,
105 2017; 2019). Using the same porosity doubling example, the different coordination number
106 models reviewed in van Antwerpen et al. (2010) predict decreases in k_s that vary only by a factor
107 of ~ 2 between.

108

109 2.1 Radiative thermal conductivity vs. regolith porosity

110 The thrust of this work is to determine the relationship between k_r and porosity (or inter-
 111 particle void fraction) of a particulate regolith. As previously mentioned, different models use
 112 different theoretical frameworks to approximate this relationship and thus lead to appreciably
 113 different results, particularly for regoliths with high macroporosity that might be found in
 114 microgravity environments such as small bodies (Murdoch et al., 2015). It is useful to summarize
 115 here the general approximation that is used as the starting point for radiative heat transfer in
 116 sphere beds — layers of spheres are approximated as a series of parallel plates (e.g., Wesselink,
 117 1948). The general formulation is:

118
 119 (Eq1)

$$k_r = 4\sigma F d_p \bar{T}^3$$

120
 121
 122 where σ is the Stefan-Boltzmann constant, F is a radiative exchange factor, d_p is the sum of the
 123 plate half thickness and the gap half thickness (later this will be particle diameter when we use
 124 this to describe sphere beds), and \bar{T} is the mean temperature (Wesselink, 1948; Jakob, 1957). In
 125 the true case of heat transfer by radiation across a series of parallel plates, F is simply a function
 126 of hemispherical emissivity (ϵ) of the plates, i.e., $F = \epsilon/(2 - \epsilon)$.

127 Approximating a packing of regolith particles as a series of perfectly opaque layers is
 128 obviously a huge oversimplification. The radiative exchange factor, F , serves to bridge the gap
 129 between this approximation and the bed of particles that constitutes a regolith. Many have sought
 130 to define the radiation exchange factor or sought other novel methods to approximate or directly
 131 model heat transfer in packed beds of spheres, especially in literature related to pebble bed
 132 nuclear reactors (van Antwerpen et al., 2010; de Beer et al., 2018; Calderón-Vásquez et al.,
 133 2021) and other industrial applications (Vortmeyer, 1979; Tausendschön and Radl, 2021).
 134 However, many of these studies have only considered packings across a narrow range of porosity
 135 values (e.g., $\sim 0.4-0.5$), which are in general too narrow for planetary science applications. Upon
 136 finding a small sensitivity in F to porosity within this range, some concluded that porosity was
 137 not worth consideration compared to other factors that tend to vary more widely in industrial
 138 applications, such as the emissivity (e.g., Singh and Kaviany, 1994).

139 Recent regolith thermal conductivity models have suggested that F could be quite
 140 sensitive to porosity across the full range of regolith microporosities relevant to planetary
 141 regolith, yet they differ considerably in their predictions. Sakatani et al. (2017) assume that F is
 142 chiefly related to the length of the void spaces present between particles. The voids are
 143 approximated as having a spherical shape; F is used to relate particle diameters in Equation 1 to
 144 porosity:

145
 146 (Eq2)

$$F = \frac{\epsilon}{2 - \epsilon} \zeta \left(\frac{\phi}{1 - \phi} \right)^{1/3}$$

147

148 where ϕ is the regolith porosity and ζ is an empirical correction coefficient obtained from
 149 experimental data. Laboratory measurements of the bulk thermal conductivity of glass beads
 150 (Sakatani et al., 2017) and basaltic particles (Sakatani et al., 2018) indicated that ζ may have a
 151 particle size dependence. The exact physical cause of this is not clear, however it may be due to a
 152 breakdown in the assumption that each particle is an independent scatterer of light as particle
 153 size approaches the dominant thermal infrared wavelengths (Wada et al., 2018).

154 Glundlach and Blum (2012; 2013), to the contrary, rely on the assumption that F is
 155 controlled by the mean free path of the photon:

156

157 (Eq 3)

158
$$F = \epsilon e_1 \frac{\phi}{1 - \phi} * \left[\frac{2}{3} \right]$$

159 where e_1 is an empirical constant, the value of which was estimated to be ~ 1.33 or $\sim 4/3$ based on
 160 simulations of gas particle diffusion through porous media by Skorov et al. (2011).

161 The value of $2/3$ in brackets is used in Gundlach and Blum (2012) based on a formulation for F
 162 from Merrill (1969). However, in a follow-up work (Gundlach and Blum, 2013) the authors omit
 163 this additional factor of $2/3$ in favor of a formulation of F referenced to Schotte (1960).

164 Interestingly, $e_1 \frac{\phi}{1 - \phi}$ is nearly identical to the equation for the hydraulic diameter of a pore in a
 165 porous medium. A recent model by Wood (2020) uses a similar formulation and more clearly
 166 ascribes it to the Kozeny-Carman law for viscous fluid flow in a porous medium.

167 Another noteworthy model for radiative thermal conductivity in a sphere bed was
 168 presented by van Antwerpen et al. (2012). Radiative conductivity is broken into two terms to
 169 describe heat transfer between directly adjacent spheres (“short-range”) and radiation between
 170 non-adjacent spheres (“long-range”). They also include a sphere non-isothermality correction
 171 expression, based on the formulation introduced by Singh and Kaviany (1994) that we will
 172 discuss in the next section. The formulations for F for short-range radiative heat transfer is a
 173 function of the number of surrounding spheres (i.e., average coordination number), the view
 174 factor between touching spheres, the average contact angle (i.e., the average angle between the
 175 net heat flow vector and the vector connecting two spheres), and the emissivity of the spheres.
 176 For long-range radiation, F depends on the decay in average sphere-to-sphere view factor with
 177 distance. They use an average sphere distance and an average view factor, based on a plot of
 178 view factor versus distance, and an empirical correction factor, to the calculation of long-range
 179 F . The decay in view factor with distance would depend on the packing density of the sphere
 180 bed. Given that this model was tailored to describe pebble bed nuclear reactors, the porosity is
 181 set to approximately 0.39. In order to apply their model to our work, we would need to find a
 182 new expression for the view factor decay with distance as a function of sphere bed porosity,
 183 which is challenging. As such, we do not use their model directly but will refer later to the
 184 concept of long-range and short-range radiation in the discussion of our results.

185 Finally, a recent formulation for F was obtained from a numerical view-factor matrix
 186 model (Wu et al., 2020). The study specifically focuses on the effect of porosity:

187

188 (Eq 4)

189
$$F = \varepsilon \left[a + b \left(\frac{\phi}{1 - \phi} \right)^c \right]$$

190 where empirical constants $a = 0.8049$, $b = 0.3728$, and $c = 1.6214$ produce an excellent fit to
 191 their numerical results for porosity values in the range of ~ 0.26 – 0.51 .

192

193 2.2 Radiative thermal conductivity and the non-isothermality effect

194 The simplified form of radiative thermal conductivity of a series of parallel plates in
 195 Equation 1 relies on the following approximation:

196

197 (Eq 5)

198
$$\frac{(T_a^4 - T_b^4)}{(T_a - T_b)} \approx 4\bar{T}^3$$

199 where T_a and T_b are the temperatures of two adjacent plates and \bar{T} is the mean temperature
 200 (Wesselink, 1948). This approximation is valid if two assumptions are true: the temperature
 201 difference between the two plates is much smaller than the mean temperature, and the
 202 temperature gradients within each plate are much smaller than the temperature difference
 203 between two adjacent plates (i.e., each plate is approximately isothermal). The first assumption is
 204 almost universally valid in planetary regoliths, as exhibited by a simple example: If $T_a = 300\text{ K}$
 205 and $T_b = 350\text{ K}$, which is likely a much larger temperature gradient than would ever be found
 206 between two adjacent regolith particles, the two sides of Equation 5 differ only by an error of
 207 $\sim 0.6\%$. Thus, this assumption would almost universally be valid in cases of planetary regolith,
 208 even under extreme cases, such as in the uppermost particle layers of the lunar regolith (e.g.,
 209 Henderson and Jakosky, 1994).

210 The second assumption that the plates or the particles are essentially isothermal was
 211 recently found to be violated in some planetary regolith cases (Ryan et al. 2020) and has been
 212 described for sphere beds in industrial applications by several others (Breitbach and Barthels,
 213 1980; Robold, 1982; Singh and Kaviany, 1994; van Antwerpen et al., 2012). The magnitude of a
 214 temperature gradient across a plate or particle, compared to the overall gradient across the series,
 215 is related to the thickness of the plates and to their thermal conductivity. This assumption of plate
 216 isothermality is generally valid when this approximation is applied to planetary regoliths because
 217 most regolith particles on commonly studied bodies like the Moon and Mars are small (sand or
 218 smaller) and are made out of geologic materials with relatively high thermal conductivity values.
 219 However, Ryan et al. (2020) showed that regolith particles on rubble-pile asteroids like Bennu
 220 and Ryugu could have significant thermal gradients due to their large size (\sim cm scale) and
 221 apparently low thermal conductivity (e.g., Rozitis et al., 2020; Shimaki et al., 2020; Cambioni et
 222 al., 2021). This so-called non-isothermality effect acts to reduce the temperature-dependence of
 223 the bulk radiative thermal conductivity. That is, equation 1 no longer follows T^3 and instead
 224 relies on the inclusion of a non-isothermal correction factor, f_k . The non-isothermality effect was
 225 parameterized by Singh and Kaviany (1994) and van Antwerpen et al. (2012) as a function of a
 226 dimensionless parameter, Λ_s :

227

228 (Eq 6)

$$229 \quad \Lambda_s = \frac{k_m}{4D\sigma T^3}$$

230 where D is the particle diameter (or, the Sauter mean particle diameter in the case of
 231 polydisperse packings, Ryan et al. 2020). The non-isothermal correction factor, f_k is then
 232 calculated as:

233

234 (Eq 7)

$$235 \quad f_k = a_1 \tan^{-1} \left(a_2 \left(\frac{1}{\Lambda_s} \right)^{a_3} \right) + a_4$$

236

237 where a_1 , a_2 , a_3 , and a_4 are empirical constants. Ryan et al. (2020) calculated new values for
 238 these constants using finite element method (FEM) simulations of heat transfer through dense
 239 random packings of monodisperse and polydisperse spheres with porosities spanning a relatively
 240 narrow range (~ 0.35 – 0.39).

241

242 Our equation for radiative conductivity now reads:

243 (Eq 8)

$$244 \quad k_r = 4\sigma F(\varepsilon, \phi) f_k(k_m(T), D, T) d_p \bar{T}^3$$

245

246

247 **3 Methods**

248 **3.1 Finite Element Model**

249 We use the FEM to model heat transfer in regolith that is approximated as a 3D meshed
 250 geometry of spheres, where each sphere represents a regolith particle. A constant heat flux is
 251 applied to a plate on one side of a three-dimensional, parallelepiped-shaped geometry of packed
 252 spheres while a constant temperature boundary condition is applied to a plate on the opposite
 253 side (Figure 1). Once a steady state temperature distribution is achieved, the bulk thermal
 254 conductivity of the system can be calculated from the temperature difference between the two
 255 plates, the distance between the plates, and the applied heat flux. These methods are described in
 256 more detail in Ryan et al. (2020). As in that work, bulk radiative thermal conductivity is studied
 257 exclusively here by removing the contacts between spheres. Nevertheless, heat diffusion within
 258 any individual sphere is still modeled and is responsible for the non-isothermality effect
 259 described later.

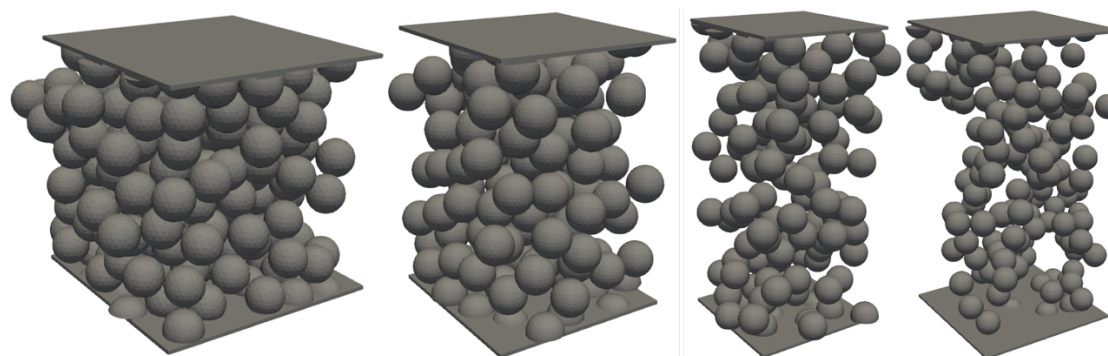
260 One key improvement that has been implemented since our previous work is the addition
 261 of periodicity. All sphere packings in this study are periodic in the two spatial directions (x and
 262 y) that are orthogonal to the direction of heat flow (z), so as to create the illusion that the

263 geometry is infinitely wide geometry, which acts to minimize boundary effects. Surface-to-
 264 surface radiative heat transfer is then made periodic by modifying the ray tracing step that is
 265 performed to determine which surface mesh elements are visible to each other for heat transfer.
 266 During this step, the surface mesh geometry is temporarily duplicated and translated to the eight
 267 possible locations immediately surrounding the original geometry (i.e., +x, +x +y, +y, +x -y,
 268 etc.) in order to create one layer of heat transfer periodicity.

269 All simulations were conducted with monodisperse sphere packing geometries with
 270 sphere diameters ≤ 1 cm. Our model is not currently able to handle non-unitary emissivity, so in
 271 all simulations the emissivity is unitary. Additionally, surfaces are assumed to have a Lambertian
 272 thermal emission phase function. The thermal conductivity of the sphere material (k_m) was varied
 273 between 0.025 and 30 W m⁻¹ K⁻¹. Prescribed heat flux values were chosen based on the thickness
 274 and bulk thermal conductivity of each sphere bed in order to minimize thermal gradients across
 275 the entire bed to <10 K. Flux values were in the range of ~2.5–10 W m². Sphere bed thicknesses
 276 were within the range of ~4–14 cm. Thicker beds were necessary for higher porosity packings in
 277 order to better capture to minimize edge effects caused by the boundary plates. In order to
 278 determine optimal geometry thicknesses, we performed a series of tests of varying thickness with
 279 different packing types and different packing density (porosity) values. The results of this are
 280 described in the supplemental materials.

281

282



283

284 **Figure 1.** Random packing examples used in this work. The average porosity values are (left to
 285 right) 0.47, 0.60, 0.71, and 0.81. All packings are periodic in the lateral directions. The packing
 286 methods used (left to right) are Optimized Dropping and Rolling, Ballistic Deposition (single
 287 sphere), Random Sequential Packing, and Ballistic Deposition (four-sphere clusters).

288

289 We utilized an improved method for extracting bulk thermal conductivity from the
 290 numerical simulation results. In the previous work (Ryan et al., 2020), the bulk thermal
 291 conductivity was determined from the steady-state temperature difference and distance between
 292 the two end plates and the prescribed heat flux using Fourier’s law. In this work, we found that
 293 the porosity within a given sphere packing could in some cases be highly variable and thus
 294 decided to instead calculate local conductivity in discrete slices of each geometry. To do so, the
 295 output steady-state temperature solution mesh is divided into 1 cm thick layers (equivalent to 1
 296 sphere diameter in most simulations). The average temperature of the top and bottom plane of
 297 each slide is calculated. The difference between the temperatures of these two planes provides us

298 our ΔT . With this, the known prescribed heat flux (q), and the known slice thickness (Δx), the
 299 local bulk thermal conductivity for each slice is calculated with Fourier's law:

300

301 (Eq 9)

$$302 \quad k_r = q \frac{\Delta x}{\Delta T}$$

303

304

305 Bulk thermal conductivity is then converted to the non-dimensional radiative exchange factor
 306 using:

307

308 (Eq 10)

$$309 \quad F = \frac{k_r}{4\sigma d_p \bar{T}^3}$$

310

311 where \bar{T} is the mean temperature within a given slice.

312 The local porosity is also calculated for each individual slice. The final results are
 313 presented as the mean values of F versus porosity from all slices within a sphere packing
 314 geometry, excluding a few (1–3) slices nearest to the boundary plates (depending on geometry
 315 thickness) where it was found that F was consistently lower than in the central region due to edge
 316 effects (Figure S1). Error bars in F vs porosity space are the maximum and minimum respective
 317 values found among the slices within a given geometry, again excluding slices suspected to be
 318 affected by edge effects.

319 The value of the non-isothermality correction factor, f_k , is calculated like in Ryan et al.
 320 (2020) by comparing pairs of thermal simulation results — one where the non-isothermal effect
 321 is negligible and another where it is expected to be significant ($\geq 1\%$). Ryan et al. (2020)
 322 assumed that the non-isothermal effect is only significant when $1/\Lambda_s > \sim 0.04$, based on previous
 323 work by van Antwerpen et al. (2012). Our approach in this work is more conservative, such that
 324 we use simulation results for F where $1/\Lambda_s \leq 0.0035$ as our baseline values against which we
 325 determine the non-isothermal correction factor. In these baseline cases with negligible
 326 intraparticle non-isothermality, we use a material thermal conductivity of $k_m = 30 \text{ W m}^{-1} \text{ K}^{-1}$.
 327 Subsequent simulations are then performed with lower values of k_m , which increases $1/\Lambda_s$ and
 328 creates non-isothermality within particles. The value of f_k is then calculated by comparing the
 329 resulting value of F where $k_m < 30 \text{ W m}^{-1} \text{ K}^{-1}$ to the previously determined baseline value of F
 330 where $k_m = 30 \text{ W m}^{-1} \text{ K}^{-1}$:

331

332 (Eq 11)

$$333 \quad f_k = \frac{F_{k_m < 30}}{F_{k_m = 30}}$$

334 Uncertainty in f_k is calculated using the same values used for the error bars in F , that is
335 $f_{k,\text{maxerror}} = (F_{k_m < 30, \text{max}} / F_{k_m = 30, \text{min}})$ and respectively for the minimum error value.

336

337

338 3.2 Sphere packing methods

339 In order to determine if the details of a random packing are influential on the bulk
340 radiative conductivity, we utilized several methods to generate the random sphere packings with
341 different porosity values (Figure 1). The Ballistic Deposition method begins with a seed sphere
342 or a simple seed cluster of spheres in the periodic domain space. New spheres or sphere clusters
343 are then brought from a random location outside of the domain and following a random
344 trajectory. If the sphere or cluster touches an existing sphere within the domain, it sticks
345 immediately. The new addition is kept as long as it does not violate periodicity. This process is
346 repeated many times until the cluster has grown to fill the periodic domain space so that any new
347 spheres or clusters that are brought in are rejected, even after a very large number of attempts
348 ($\sim 10^5$). Different porosity values may be achieved depending on if individual spheres or sphere
349 clusters are used in the deposition. For example, single sphere deposition can be used to generate
350 packings with porosities in the range of ~ 0.59 – 0.61 . Deposition by clusters that contain 2 spheres
351 leads to porosities of ~ 0.67 , whereas 3-sphere clusters lead to ~ 0.72 and 4-sphere clusters lead to
352 ~ 0.74 and higher.

353 The Random Sequential Packing method quite simply involves the introduction of a new
354 sphere in the 3D periodic domain space in some random location. If the sphere does not overlap
355 an existing sphere and does not violate periodicity, it is kept. The spheres are not touching each
356 other in this method, so it is not as representative of a natural regolith. However, it has the
357 flexibility of a wide range of achievable porosity values. The densest possible packing that we
358 have achieved with this method has a porosity of ~ 0.63 .

359 The Optimized Dropping and Rolling is the same as that described by Hitti and Bernacki
360 (2013) but modified to add periodicity. Spheres are dropped into the periodic domain space from
361 above and roll into a stable position in order to achieve a loose random packing (porosity ~ 0.43 –
362 0.45).

363 Finally, the method by Ringl et al. (2012) is used, where spheres are sequentially attached
364 to pre-existing spheres in spaces in the geometry with low local packing fraction values (see also
365 Ballouz et al., 2021). The method can be terminated once a desired packing density is reached, or
366 allowed to run until no further sphere sites can be found after a large number of attempts, as with
367 the Random Sequential Packing Method. We achieved packings with porosity values as low as
368 ~ 0.57 with this method.

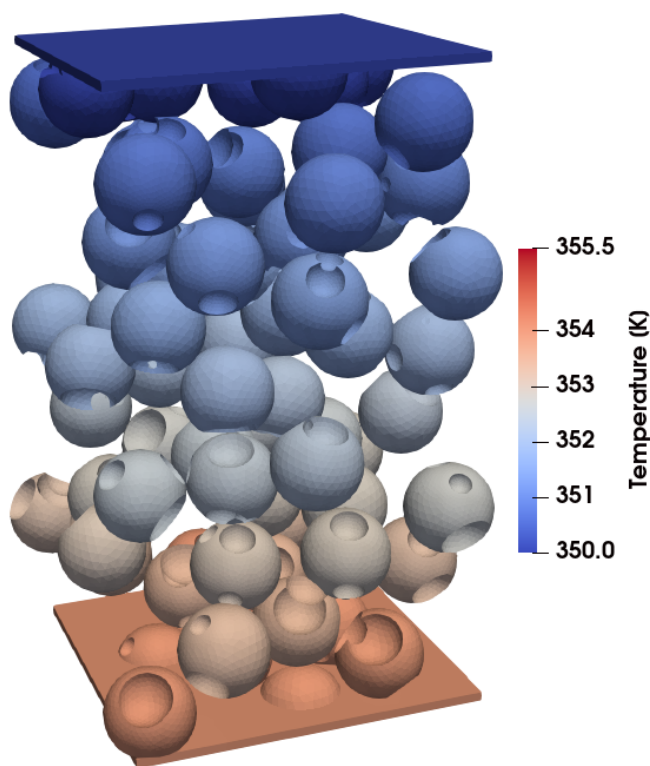
369 Ordered cubic packing structures (a.k.a. “regular” or “structured” packings) were also
370 tested in order to examine low-porosity packings. Simple cubic, body-centered cubic, and face-
371 centered cubic packings have porosity values of ~ 0.48 , ~ 0.32 , and ~ 0.26 , respectively. The
372 diameters of the spheres in these three packings were then reduced in order to achieve higher
373 porosity values while maintaining an ordered arrangement, although the spheres in those
374 configurations are no longer touching and thus the packings are not possible in nature.

375

376 3.3 Method for investigating particle roughness

377 In addition to the measurements of monodisperse particles described above, a limited set
 378 of simulations were conducted with non-spherical particles as preliminary assessment of the
 379 effects of particle angularity. Random packings of spheres were generated using the methods
 380 described above. The spheres were then “roughened” by the addition of craters to the sphere
 381 surfaces. The craters were placed on each sphere by randomly choosing a surface coordinate on
 382 the sphere for the placement of another small sphere that served as a subtractive object. In order
 383 to qualitatively maximize the roughness induced by these craters on the host spheres while
 384 maintaining some semblance of the original spherical particle shape, these spherical section
 385 craters were constrained to have radii between 1/4 and 2/3 the diameter of the host sphere.
 386 Finally, the spherical section craters were restricted to be placed within $\pi/3$ radians of the poles
 387 of the host spheres pointing in the direction of heat flow, in an attempt to maximize the effect of
 388 the roughness on heat transfer in a manner similar to asteroid thermal models where spherical
 389 section craters are used to approximate topographic roughness (e.g., Spencer, 1990; Rozitis and
 390 Green, 2011).

391



392
 393 **Figure 2.** Particles with surfaces roughened by the addition of spherical section craters. The
 394 colors represent the final, steady-state temperatures.

395

396

397

398

399 3.4. Preparation of experimental data for comparison

400 The recent experimental datasets by Sakatani et al., 2017 and 2018 are ideal for
 401 comparing to our model results, given that they measured somewhat coarse particles (up to ~1
 402 mm diameter), where radiative thermal conductivity is significant, using a well-established
 403 method (line heat source, e.g., Presley and Christensen, 1997). Measurements of bulk thermal
 404 conductivity are made with glass spheres and with the JSC1A lunar regolith simulant in different
 405 size fractions and at different temperatures, in the range of ~250–330 K. The relative
 406 contributions of the radiative and solid conductivity terms are determined by fitting their regolith
 407 thermal conductivity model to the temperature dependent results, where the radiative
 408 conductivity term is assumed to be proportional to T^3 and the solid conductivity term is assumed
 409 to be proportional to the conductivity of the particulate material, which is typically only
 410 minimally temperature-dependent (e.g., Opeil et al., 2020). Sakatani et al., 2017 and 2018
 411 express their results in terms of tunable parameters for solid conductivity (ξ , xi) and radiative
 412 conductivity (ζ , zeta, equation 2). The model of Sakatani et al., 2017 is in good agreement with
 413 our numerical results for porosities $\lesssim 0.60$ when ζ is ~1.25–1.4 and emissivity is unitary. Their
 414 experimental results for the two largest particle ranges tested (355–500 and 710–1000 μm) show
 415 that ζ is consistently lower in the JSC1A samples compared to the glass beads (Sakatani et al.,
 416 2018, see Fig. 13b within). The absolute values of radiative conductivity and F show that their
 417 measurements are significantly lower than our model results. Below, we re-evaluate the way that
 418 radiative conductivity was calculated from their experimental data in an effort to reassess how
 419 well their measurements agree with our results.

420 In order to calculate radiative thermal conductivity and radiative exchange factor from
 421 the experimental measurements of bulk conductivity by Sakatani et al. (2018) for comparison to
 422 our work, one must have some knowledge of the sample particle size, porosity, emissivity, and
 423 the thermal conductivity of the individual sample particles. We will revisit the values chosen for
 424 each of these parameters.

425 First, a single, representative particle size must be assumed for each experimental sample.
 426 The two coarsest samples tested in JSC1-A had particle sizes of 355–500 and 710–1000 μm .
 427 These size bins are relatively large; they each span ~40% in particle size. Sakatani et al. (2018)
 428 used the average of the two bounding values for each size range in their data interpretation
 429 calculations (427 μm and 855 μm , respectively). Conversely, the bulk thermal conductivity of
 430 the entire JSC1-A regolith (unsorted) was found to be well-represented by the volumetric median
 431 particle size. This result was assumed to be valid for both the solid and radiative thermal
 432 conductivity terms; the experimental data set is not comprehensive enough to constrain the
 433 effective particle size of the two thermal conductivity components separately. Alternatively,
 434 Ryan et al. (2020) found that the Sauter mean particle size is representative of the bulk for the
 435 purpose of calculating effective radiative thermal conductivity. In many cases, the Sauter mean
 436 and the volumetric median particle size are very similar, including in the sphere packings studied
 437 by Ryan et al. (2020). We calculate both for the two aforementioned sample size fractions,
 438 assuming that the distribution within each size fraction is the same as in the bulk sample,
 439 parameterized using log-normal distribution by mass with distribution parameters $\mu = 4.66$ and
 440 $\sigma = 0.972$ in units of $\ln(\mu\text{m})$ (Sakatani et al., 2018). In both cases, the volumetric median and
 441 Sauter mean particle sizes are within a few percent of each other. We arbitrarily choose the
 442 volumetric median as the new effective particle size for the two samples in our calculations of
 443 radiative thermal conductivity and radiative exchange factor. As such, the effective particle size

444 of the 355–500 μm sample is 412 μm rather than the original range-based mean value of 427 μm .
445 The 710–1000 μm value is 816 μm rather than 855 μm .

446 The porosity of each sample was determined by Sakatani et al. (2018) from the measured
447 bulk density (from measured sample mass and sample container volume) and an assumed
448 particle density (a.k.a. specific gravity) value of 2900 kg m^{-3} , which is an average measured
449 value for JSC1A (McKay et al., 1994; Zeng et al., 2010). However, the measured bulk density
450 and porosity values vary substantially between sample size fractions, from 1540 kg m^{-3} and
451 porosity of 0.47 in the smallest size fraction (53–63 μm) to 980 kg m^{-3} and porosity of 0.66 in the
452 largest size fraction (710–1000 μm). All samples were loaded into the sample container using the
453 same methods; each sample was poured into the container and then tapped. Thus, it is not readily
454 apparent why the packing density values should differ so significantly. Rather, we suspect that
455 the assumption of a constant particle density between the different size fractions is responsible
456 for the different measured bulk density values.

457 The JSC1-A lunar regolith simulant, described as a volcanic ash of basaltic composition
458 (McKay et al., 1994), was produced by crushing and impact milling basalt cinders or “basaltic
459 welded tuff” (Taylor et al., 2005) from a cinder ash quarry on the flank of Merriam Crater cinder
460 cone in the San Francisco Volcanic Field (Sibille et al., 2006); in particular, it was selected for its
461 high glass content ($\sim 50\%$). Scanning electron micrograph images of smaller size fractions ($< \text{few}$
462 hundred μm) show that the “glassy particles invariably display broken vesicles with sharp edges”
463 (McKay et al., 1994). The larger particles ($\sim 500\text{--}1000 \mu\text{m}$) have abundant vesicles that are
464 visible by eye or hand lens. As such, it may be expected that vesicularity, or porosity, should
465 vary between size fractions, where the larger particles are more likely to contain complete
466 vesicles in their interiors and edges. Tamari et al. (2005) for example found that particle density
467 of a scoria varied as a function of particle sizes in the range of $\leq 4.75 \text{ mm}$ to $< 74 \mu\text{m}$. Conversely,
468 Zeng et al. (2010) measured the specific gravity of JSC1A in two size fractions, separated by the
469 75 μm sieve, and found no difference. Both of these studies utilized a water pycnometry method,
470 in which water is likely to penetrate into some of the vesicles, excluding them from the particle
471 density analysis and thus leading to density overestimates. We suspect that the fraction of JSC1-
472 A larger than 75 μm measured by Zeng et al. (2010) still contained abundant crushed, fine
473 particles that did not contain closed vesicles and thus the measurement result was insensitive to
474 any larger particles that did contain closed vesicles. Following the particle size weighted mass
475 distribution for JSC1-A in Sakatani et al. (2018), the sample that is $> 75 \mu\text{m}$ tested by Zeng et al.
476 (2010) would have consisted of 80% by mass particles smaller than 300 μm .

477 No other information on the particle density of the coarser particles in JSC1-A could be
478 found in the literature. Direct measurement of the particle density should be conducted with a
479 method that takes all vesicles into account, including those that may not be penetrated by water
480 (e.g., Garboczi, 2011). Nonetheless, we performed a new water pycnometry measurement of the
481 four size fractions used in Sakatani et al. (2018). A small but significant density decrease is noted
482 in the larger size fractions. However, we suspect that these values still over-estimate the true
483 density, given that water certainly filled pores along the edge of the sample and may have also
484 penetrated interior pores, depending on the degree of pore connectivity. For example, if we
485 assume that all samples have the same porosity of 0.45, which would be a very loose random
486 packing, the microporosity values of the two largest size fractions would be approximately 0.30
487 and 0.39 (Table S4 and S5). As such, we will re-evaluate the Sakatani et al. 2018 results with
488 these newly measured density values but will also consider the possibility that the microporosity

489 in the larger size fractions could still be higher, such as would be the case if all samples actually
 490 had the same or similar porosity values but different microporosity values.

491 The assumed material thermal conductivity in Sakatani et al. (2018) comes from
 492 experimental measurements of a non-porous basalt and displays an inverse relationship between
 493 conductivity and temperature that is common in mineral-rich samples. However, as described
 494 above, the JSC1-A simulant is a mixture of minerals and volcanic glass. Although thermal
 495 conductivity values of felsic volcanic glasses (e.g., obsidian) can be found in the literature, we
 496 were only able to find one instance of a mafic glass measurement (Birch and Clark, 1940). The
 497 sample, as described by Birch and Law (1935) was a diabase that was melted in the laboratory
 498 and cooled to form a glass that in thin section was “quite free from crystallites...and almost
 499 entirely free from gas vesicles”. The major element concentrations are similar to those reported
 500 for the JSC1 simulant (McKay et al., 1994). The two have a similar theoretical room-temperature
 501 glass thermal conductivity calculated from their composition using the glass phonon thermal
 502 conductivity model of Choudhary and Potter (2005) ($\sim 1.19 \text{ W m}^{-1} \text{ K}^{-1}$ for the diabase glass vs.
 503 $\sim 1.14 \text{ W m}^{-1} \text{ K}^{-1}$ for the JSC1A). This similarity indicates that the diabase glass is a sufficient
 504 compositional match to serve as a thermal conductivity analog for the glass component of the
 505 JSC1-A. We performed a linear least-squares fit to the thermal conductivity data for the diabase
 506 glass provided from 0–300° C in Birch and Clark (1940), obtaining $k_{\text{glass}} = 0.846 + 1.11e-3 * T$
 507 where T is temperature in Kelvin. We ultimately combine this thermal conductivity equation
 508 with the basalt equation used in Sakatani et al. (2018) to account for the approximately 50/50
 509 ratio between glass and minerals, leading to the final expression for JSC1A simulant particle
 510 with no microporosity, $k_{\text{sim}} = 1.62 + 7.61e-3 * T$. Next, if we assume that the particles are
 511 somewhat porous, as described above, we must also attempt to account for the effects of
 512 microporosity on k_{sim} . Several empirical datasets exist in the literature to describe the effects of
 513 porosity on thermal conductivity (e.g., Woodside and Messmer, 1961b; Flynn et al., 2018). We
 514 ran a simple model of a block with randomly placed nonconnected spherical voids in order to
 515 determine the effects of vesicle-like porosity in a geologic material (Figure S2). The size of the
 516 voids was increased to increase porosity, with the simplification that radiative heat transfer in the
 517 voids is negligible. We found this simplification to be valid to within a few percent at the
 518 relatively low temperatures used in the Sakatani et al. (2018) measurements. The model resulted
 519 in the following correlation to adjust a material thermal conductivity value to account for the
 520 presence of vesicular microporosity: $k_m^* = k_m * (0.466\phi^2 - 1.496\phi + 1.0)$. This equation is
 521 applied to k_{sim} when microporosity is included.

522 For the assumed emissivity, we use a value of 0.90, rather than the original value of 1.0
 523 used in Sakatani et al. (2018). Typical basalt emissivity spectra, such as from the ASU spectral
 524 library (Christensen et al., 2000) and the Salisbury and d’Aria (1992), show an integrated value
 525 of ~ 0.95 . However, those values of ~ 0.95 are for directional emissivity, typically normal or near-
 526 normal emission angle, whereas radiative heat transfer between surfaces is controlled by the
 527 hemispherical emissivity. Hemispherical emissivity tends to be smaller than directional
 528 emissivity due to a roll-off in emissivity at higher emission angles on most surfaces, except those
 529 that are extremely rough (perfectly Lambertian, Warren et al., 2019, Figure 16 within). With
 530 such a roll-off, the integral of the emission half-space is necessarily smaller than the normal
 531 emissivity. The ratio of hemispherical-to-normal emissivity for a non-metallic solid with a
 532 normal emissivity of 0.95 is approximately 0.94, according to (Touloukian and DeWitt, 1972).
 533 Thus, we adopt a nominal value for hemispherical emissivity of 0.90.

534 With all of the aforementioned revised assumptions, new values for F , ζ , and ξ are
 535 calculated by fitting the model of Sakatani et al. (2017; 2018) to the bulk thermal conductivity
 536 results for a given sample size fraction from Sakatani et al. (2018). ζ and ξ are varied as free
 537 parameters to achieve the optimal least-squares fit to the temperature-dependent experimental
 538 data. This approach to constrain these parameters is possible due to the difference in temperature
 539 dependence between the radiative and solid conductivity terms, which are tuned by ζ and ξ ,
 540 respectively. The value of F is calculated from the best fit value of ζ using Equation 2. The
 541 results are shown in Tables S4 and S5, in comparison to the original values.

542 The values of F , which are not dependent on assumed porosity, have increased compared
 543 to the original values, but otherwise do not change with assumed porosity value. That is not to
 544 say that F is not a function of the porosity of a particulate assemblage; it certainly is. Rather, the
 545 value of F determined from experimental data is independent of the experimenter's knowledge of
 546 the sample porosity. The values of ζ and ξ , on the other hand, are affected by our knowledge (or
 547 assumptions) of sample porosity. With increasing assumed sample porosity, ζ *must* decrease to
 548 compensate and maintain the same values of F and k_r . Conversely, ξ must decrease with
 549 increasing porosity to compensate for a decrease in assumed particle coordination number so as
 550 to maintain the same value of k_s .

551 Finally, it should be noted that when these values of F are compared to the results of our
 552 numerical simulations, the difference in assumed emissivity must be accounted for. In our
 553 simulations, emissivity=1, whereas we now assume that the Sakatani et al. (2018) results are for
 554 particles with emissivity=0.9. Because F is a function of emissivity, we must adjust the
 555 experimental values of F in order to compare to our simulation results. We will assume that F is
 556 proportional to $\varepsilon/(2 - \varepsilon)$, based on the parallel-plates heat transfer approximation (e.g., Sakatani
 557 et al., 2017) and thus calculated an adjusted value of $F^* = F * (2 - \varepsilon)/\varepsilon$. The original values of
 558 F are shown in Tables S4 and S5, while the adjusted F^* values are shown in later figures.

559

560 4 Results

561 The radiative exchange factor (F) values determined from all simulations where non-
 562 isothermality is assumed to be negligible (i.e., where $k_m = 30.0 \text{ W m}^{-1} \text{ K}^{-1}$) are shown in Figure 3
 563 and summarized in Tables S1 and S2. Given that the random packings and ordered packings are
 564 systematically offset from each other, we fit separate empirical functions to them using Equation
 565 4. The coefficients for the random packing fit line are $a=0.739$, $b=0.629$, and $c=1.031$. This trend
 566 line captures all random packing data points with an uncertainty of $\pm 10\%$. Uncertainty should be
 567 increased to $\pm 25\%$ for porosity values $> \sim 0.65$ in order to capture all data points, error bars, and
 568 regular packing data points (Figure S3). The regular packing data points are fit well with the
 569 following coefficients: $a=0.773$, $b=0.419$, and $c=1.180$. The fit is shown with the data on Figure
 570 4, along with the original and revised values for F from the experimental data of Sakatani et al.
 571 (2018) and unchanged experimental data for glass beads from Sakatani et al. (2017). The full
 572 results of the reevaluation of data from Sakatani et al. (2018) are provided in Tables S4 and S5.

573 Results for simulations where solid conductivity were varied to induce the non-
 574 isothermality effect are shown in Figure 5 and in Table S3. In this work, we parameterize results
 575 as a function of $(1 - \phi)/\Lambda_s$ to incorporate the effects of porosity, whereas in previous works
 576 (Ryan et al., 2020; van Antwerpen et al., 2012; Singh and Kaviany, 1994), the non-isothermality
 577 factor was presented in terms of Λ_s or $1/\Lambda_s$. A fit to the new data uses the following function:

578

579 (Eq 12)

$$580 \quad f_k = a_1 \tan^{-1} \left(a_2 \left(\frac{1 - \phi}{\Lambda_s} \right)^{a_3} \right) + a_4$$

581 where $a_1=-0.500$, $a_2=1.351$, $a_3=0.741$, and $a_4=1.007$.

582 Finally results of the simulations where spheres were roughened by the addition of
 583 spherical section craters on their surfaces are shown in Figure 6 and Table S6. The values for two
 584 simulations with roughened spheres are compared to the same packing geometries without
 585 roughness added.

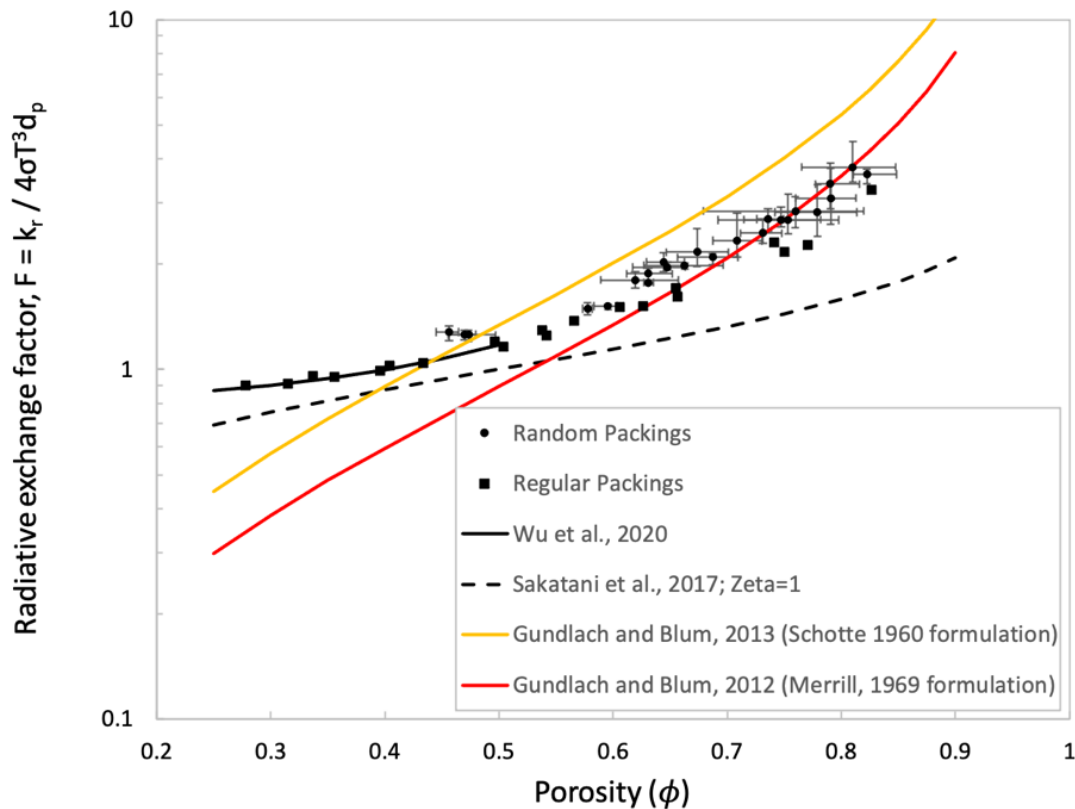
586

587

588

589

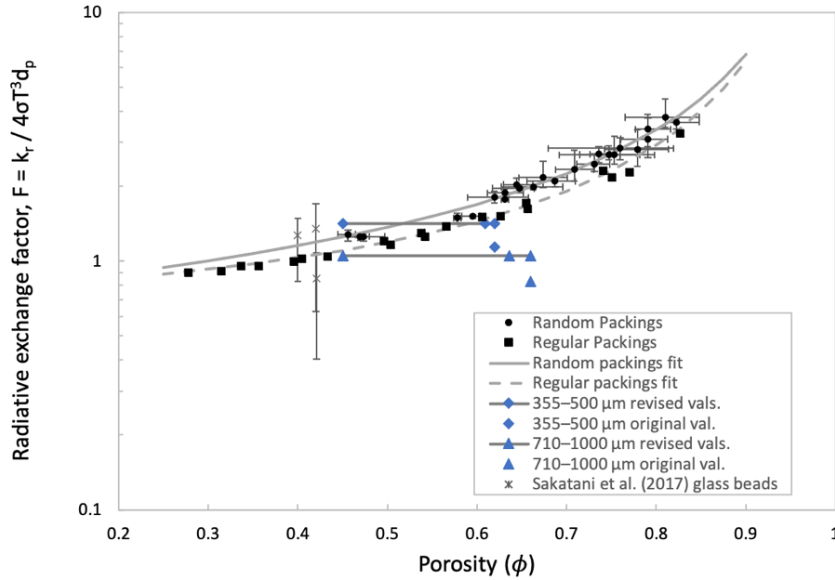
590



591

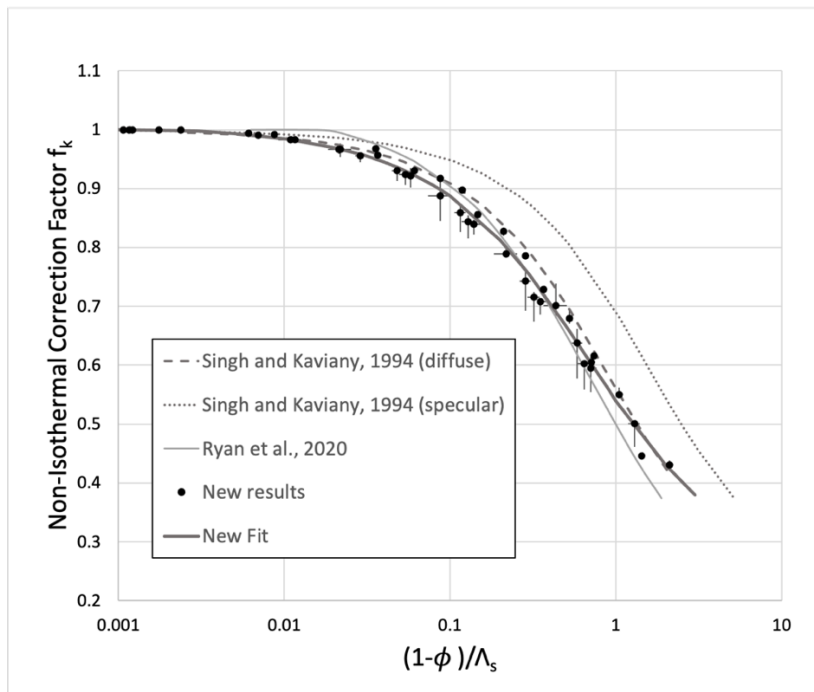
592 **Figure 3.** Numerical results for the radiative exchange factor as a function of porosity compared
 593 to models for regolith and sphere bed thermal conductivity.

594



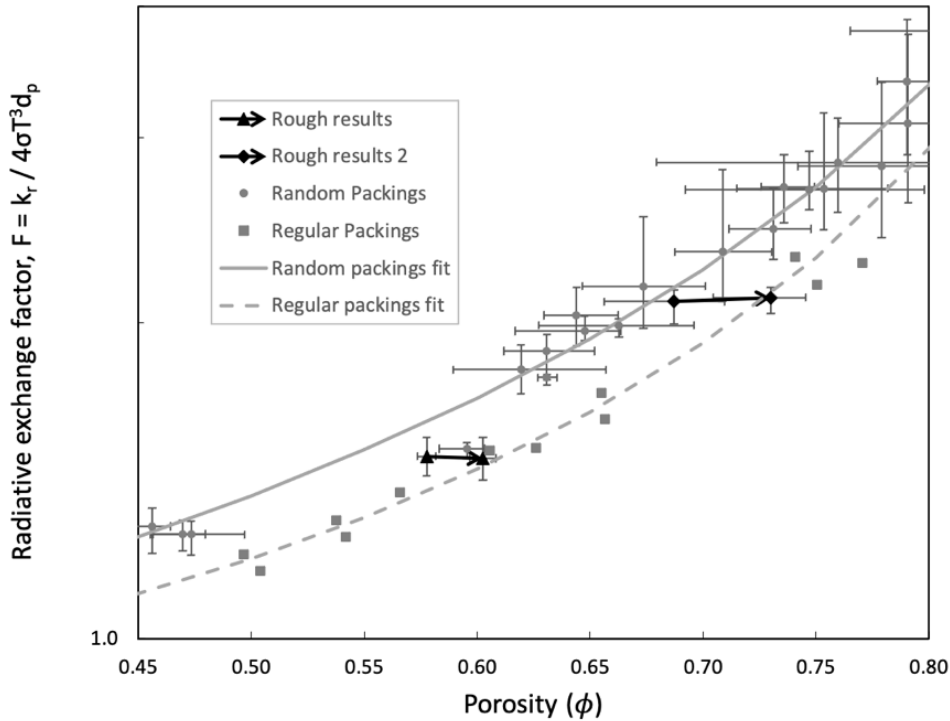
595

596 **Figure 4.** Numerical results for the radiative exchange factor as a function of porosity compared
 597 to experimental results from Sakatani et al. (2017; 2018), adjusted to F^* to account for
 598 differences in sample emissivity (~ 0.9) compared to our simulations performed with unitary
 599 emissivity. Revised values of data collected for the JSC-1A lunar simulant are compared to
 600 completely unaltered values from Sakatani et al. (2018). For the reevaluated data, we show a line
 601 connecting three porosity points (from left to right): assumed lower end value of 0.45, value
 602 water pycnometer measurements, and original value.



603

604 **Figure 5.** Results from simulations where particle non-isothermality was investigated. The new
 605 fit trendline is shown in addition to the trendlines from previous studies (Ryan et al., 2020; Singh
 606 and Kaviani, 1994).



607

608 **Figure 6.** Results for two sets of simulations where the spheres were roughened by adding
 609 spherical section craters to the sphere surfaces, overlaid on a subset of full numerical results.
 610 Arrows point from original geometry without roughened spheres to results where spheres are
 611 roughened. Values provided in Table S6.

612

613 5 Discussion

614 The calculated values of the radiative exchange factor F as a function of porosity for
 615 ordered packing are in very good agreement with the results by Wu et al. (2020), which were
 616 also determined numerically but with a matrix-based method. This gives us increased confidence
 617 that our numerical results are accurate to within a few percent. Our revised calculations of F
 618 from the experimental data of Sakatani et al. (2018) are in relatively good agreement with our
 619 numerical results. Figure 4 shows revised values of F and the range of potential porosity values
 620 for the two largest size fractions from their work. If we assume the most extreme scenario where
 621 both specimens have a true porosity of 0.45, then the two values of F bracket our results. This
 622 assumption would mean that the individual particles have high microporosity, with values of
 623 0.30 for the 355–500 μm sample and 0.39 for the 710–1000 μm sample. These microporosity
 624 values are not unusual for basaltic cinders (e.g., Robertson and Peck, 1974).

625 The results of our simulations of roughened particles provides another mechanism aside
 626 from microporosity to increase the apparent bulk porosity of a specimen without necessarily
 627 increasing the value of F . In Figure 6, it is shown that the addition of craters to the surfaces of
 628 spheres, similar to open vesicles, does not increase the value of F but does increase the measured
 629 porosity even though the packing density of the particles is unchanged. This behavior could
 630 partially explain why the experimental values of F , which were obtained with particles that are

631 known to have rough, pitted surfaces, tend to be lower than our numerical results for perfect
632 spheres. Finally, particle non-sphericity could also play a role (Garboczi, 2011). However, the
633 effects of non-sphericity on radiative conductivity have yet to be studied thoroughly
634 experimentally or numerically, though the model of Wood (2020) predicts that the radiative
635 exchange factor is directly proportional to sphericity. Nonetheless, we find that the recalculated
636 experimental values for F are in good agreement with our numerical results when considerations
637 of microporosity and particle roughness are taken into account.

638 The values of F in Figure 3 are consistently lower, by about 10–25%, in regular packings
639 than in random packings across the full porosity range investigated. We did not note any
640 systematic differences within the random packings that could be attributed to packing style or
641 whether or not the packings were physically realistic or not. We attribute the distinction between
642 random and regular packings to a difference in the relative contributions of short-range and long-
643 range radiative exchange (e.g., van Antwerpen et al., 2012). Ordered packings tend to have a
644 higher number of spheres in their immediate proximity, compared to a random packing with a
645 comparable porosity value. As such, a larger proportion of the view as seen from any surface
646 location on a given sphere will be obscured by spheres in close relative proximity (i.e.,
647 immediate neighbors). It follows that the roll-off in view factor between any two given spheres
648 in a regular packing would drop off sharply once the distance between the two spheres exceeds
649 that of the immediately neighboring spheres. This would have the effect of increasing short-
650 range radiation and decreasing long-range radiation, compared to a random packing. We
651 hypothesize that the decrease in long-range radiative heat transfer has a greater net effect than
652 the increase in short-range radiative exchange, resulting in a net decrease in heat transfer in the
653 ordered packings.

654 The overall trend between F and porosity cannot be well matched by the Sakatani et al.
655 (2018) or the Gundlach and Blum (2012; 2013) models across the full range of porosities tested.
656 The Gundlach and Blum (2013) model matches well our results for random packings for
657 porosities greater than ≥ 0.70 . This is not surprising, given that their model expression was
658 formulated using photon mean free path simulation data for porosity values exclusively in the
659 range of 0.65–0.85 (Skorov et al., 2011).

660 In order to compare the three models, we calculated predicted effective particle sizes for
661 the S-type asteroids (25143) Itokawa, (433) Eros, and (99942) Apophis and B-type asteroid
662 (101955) Bennu (Table 1). As usual, these effective particle sizes are calculated assuming that
663 the surface from which the thermal inertia value was derived is covered in a uniform blanket of
664 particulate regolith. In the absence of rocks and boulders larger than the diurnal skin depth, the
665 effective particle size is thought to reflect either the Sauter mean (Ryan et al., 2020) or the
666 volumetric median particle diameter (Sakatani et al., 2018). The presence of boulders or exposed
667 bedrock will typically shift the result towards a larger particle size, given that boulders typically
668 have a higher thermal inertia than fine regolith. The magnitude of this shift will depend on the
669 relative spatial abundance of boulders and on the difference in thermal inertia between the
670 particulate regolith and the boulder components. On a planetary body like the Moon, this
671 difference is very large (e.g., Bandfield et al., 2011). On Bennu, the difference can be very small
672 or even non-existent (Rozitis et al., 2020; Cambioni et al., 2021).

673 To calculate the effective particle size for the S-type asteroids (Table 1), we use the same
674 material properties and the same non-isothermal correction in all models so that the effect of the
675 different F versus ϕ model relationships across a range of thermal inertia values can be

676 compared. For Bennu, we assume Cold Bokkeveld-like material properties (Opeil et al., 2020)
 677 and use a nominal thermal inertia value of $200 \text{ J m}^{-2} \text{ K}^{-1} \text{ s}^{-1/2}$ and mean diurnal temperature of
 678 260 K to represent the Hokioid Crater, the location of the Nightingale sample site (Rozitis et al.,
 679 2020). For Itokawa, we use a regolith-specific thermal inertia value of $203 \text{ J m}^{-2} \text{ K}^{-1} \text{ s}^{-1/2}$ and
 680 global mean diurnal temperature of 300 K from Cambioni et al. (2019). We provide effective
 681 particle size estimates in Table 1 for regolith porosities in the range 0.40–0.90 but otherwise do
 682 not perform a robust error analysis at this time, given that the aim of this exercise is to compare
 683 nominal model predictions.

684 **Table 1.** Example predicted effective particle diameters for four asteroids using different regolith
 685 thermal conductivity models assuming regolith porosity values in the range of 0.4–0.9.

686 Predictions for Eros, Itokawa, and Apophis use S-type material properties from Gundlach and
 687 Blum (2013). Predictions for Bennu use material properties as described in Rozitis et al. (2020)
 688 with the exception of using Cold Bokkeveld thermal conductivity and heat capacity at 260 K
 689 from Opeil et al. 2020. The Sakatani model uses $\zeta = 0.68 + (7.6 * 10^{-5})/D_p$ and $\xi = 0.12$
 690 (Wada et al., 2018). For our calculations, we use Equation 4 with the fit random packing fit
 691 parameters provided in the Results section to calculate radiative conductivity. To calculate solid
 692 conductivity, we use the Sakatani et al. (2017) expression (their Equation 19); using the
 693 Gundlach and Blum (2013) solid conductivity expression provides very similar results. Thermal
 694 inertia and mean temperature values for Eros come from Gundlach and Blum (2013) and
 695 references therein. Given that the thermal inertia of Apophis is not well constrained, we calculate
 696 particle sizes for the low, middle, and high best fit values from Licandro et al. (2016) with an
 697 average temperature of 250 K (Sorli and Hayne, 2020). TI is thermal inertia in units of $\text{J m}^{-2} \text{ K}^{-1}$
 698 $\text{s}^{-1/2}$.

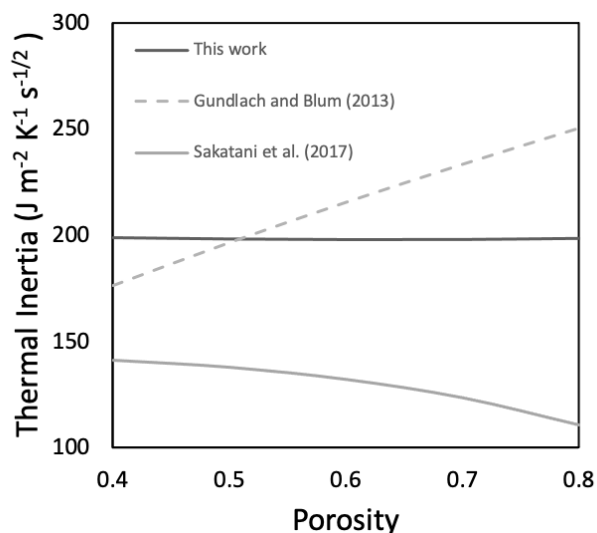
Model	Eros TI=150 (mm)	Bennu <i>Nightingale</i> TI=200 (mm)	Itokawa <i>Regolith</i> TI=200 (mm)	Apophis TI=50 (μm)	Apophis TI=275 (cm)	Apophis TI=500 (cm)
This work	4.8–4.9	8.0–8.2	5.3–5.4	450–560	1.7–1.73	5.7–5.9
Gundlach and Blum (2013)	2.8–6.0	4.5–10.6	3.0–6.7	270–312	1.0–2.2	3.2–7.8
Sakatani et al. (2017)	9.3–24	17.3–41.7	10–25	830–2580	3.4–8.3	14.4–28.7

699
 700 Our new model for random packings predicts particle sizes that fall within the range of
 701 predictions by the Gundlach and Blum (2013) model. The Gundlach and Blum model results are
 702 more sensitive to porosity than our model and lead to a wider range of predicted values, given
 703 the steeper slope in the relationship between F and porosity (Figure 3). The Sakatani model tends
 704 to predict much larger particle sizes, which is a direct result of its lower predicted values for F ,
 705 especially at higher porosities. To illustrate the relative relationships between porosity and
 706 thermal inertia, we plot the thermal inertia of 7.5 mm diameter regolith particles in Figure 7
 707 using the model parameters used to calculate the Bennu particle sizes in Table 1. Although all
 708 three models predict an increase in thermal conductivity with increasing porosity, the magnitude

709 of this increase relative to the accompanying decrease in regolith bulk density with increasing
 710 porosity causes the three models to behave very differently. The increase in conductivity with
 711 porosity in our model is approximately equivalent to the decrease in density. The Gundlach and
 712 Blum (2013) model outpaces the density decrease, whereas the Sakatani model falls behind it.

713

714



715

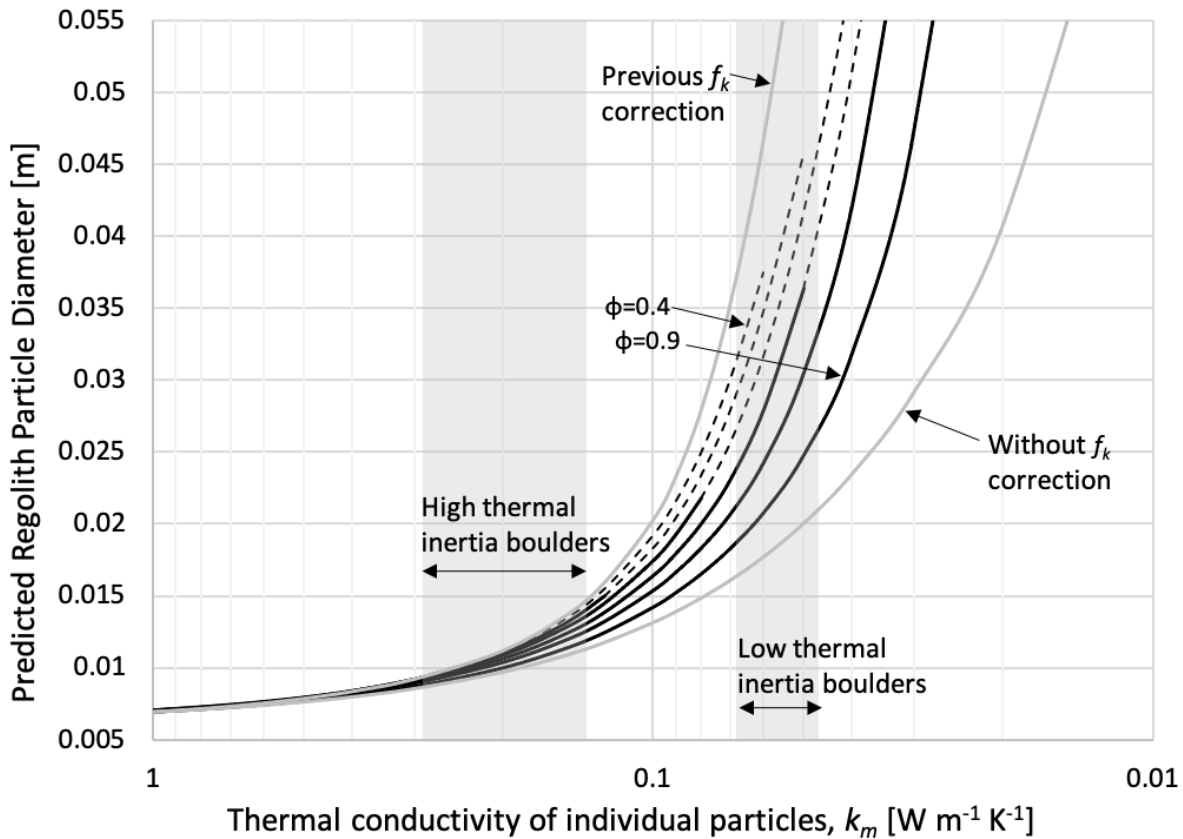
716 **Figure 7.** Calculated thermal inertia comparison for a hypothetical Bennu regolith particle of 7.5
 717 mm diameter.

718

719 Finally, we have demonstrated that the non-isothermality effect in regoliths with different
 720 porosity values can be well-described by Equation 12 (Figure 5, “New Fit”). To visualize this
 721 result compared to the previous, porosity-insensitive results, we repeat the exercise from Ryan et
 722 al. (2020) and show the predicted particle size as a function of particle thermal conductivity for a
 723 regolith on Bennu with a thermal inertia of $200 \text{ J m}^{-2} \text{ K}^{-1} \text{ s}^{-1/2}$, which is the upper end of the
 724 OSIRIS-REx Nightingale Sample site thermal inertia value calculated from Recon A mission
 725 phase data (Rozitis et al., 2020). The result is shown in Figure 8 overlain with thermal
 726 conductivity of the two Bennu boulder types, which may serve as the source material for the
 727 regolith particles at Nightingale.

728

729



730

731 **Figure 8.** Example particle size prediction for the Nightingale sample site on Bennu (thermal
 732 inertia of $200 \text{ J m}^{-2} \text{ K}^{-1} \text{ s}^{-1/2}$ at 265 K) as a function of the conductivity of the material that
 733 makes up the regolith particles (k_m). Predicted values using the new non-isothermality (f_k)
 734 correlation the effects of porosity are shown as dark black solid and dashed lines. Lines change
 735 from solid to dashed when the predicted particle size exceeds the diurnal skin depth. Lines
 736 disappear completely when the prediction exceeds two diurnal skin depths. The lines are
 737 presented in order of assumed regolith porosity, with the two end values of 0.4 and 0.9 labeled.
 738 For comparison, the predictions are shown using the previous f_k correction from Ryan et al.
 739 (2020) and without using any f_k correction. The shape of those curves is insensitive to assumed
 740 regolith porosity; skin depth cutoffs however are sensitive to porosity but were not possible to
 741 clearly plot. All model parameters are the same as described in Ryan et al. (2020) and Rozitis et
 742 al. (2020), with the following exceptions: heat capacity is taken from the measurement of the
 743 Cold Bokkeveld meteorite by Opeil et al. (2020), particle density (or microporosity) varies with
 744 particle thermal conductivity using the model by Flynn et al. (2018), emissivity=0.95, and $\zeta =$
 745 $0.68 + (7.6 * 10^{-5})/D_p$ (from Wada et al., 2018). Bennu low and high thermal inertia boulder
 746 values from Rozitis et al. (2020) were used to calculate the conductivity ranges, using the same
 747 assumptions for grain density and the relationship between porosity and microporosity described
 748 above.

749

750

751 For a particulate regolith to have a lower thermal inertia compared to its source rock
 752 material, the size of the regolith particles should be smaller than one or a few skin depths (the
 753 exact cutoff is not yet known; Ryan et al., 2020). Otherwise, particulate regolith and rock should
 754 be indistinguishable. Several pieces of useful information may be extracted from Figure 8. First,
 755 if the regolith is sourced from the high thermal inertia boulders, the particle size prediction is
 756 well-constrained and is minimally sensitive to porosity. Conversely, if the regolith is sourced
 757 from the low thermal inertia boulders, the particle size is very poorly constrained without
 758 additional information, such as an estimate of porosity. For example, if we assume that the
 759 source rock material that composes the regolith at the Nightingale site has a thermal inertia of
 760 $200 \text{ J m}^{-2} \text{ K}^{-1} \text{ s}^{-1/2}$ ($k_m \approx 0.053 \text{ W m}^{-1} \text{ K}^{-1}$), the particle size of the regolith could be anything
 761 larger than $\sim 2.25 \text{ cm}$. However, if the images could for example be used to constrain that the
 762 effective regolith particle size to smaller than 3 cm , then one could conclude that the regolith
 763 must have a porosity greater than ~ 0.7 , if we maintain the assumption that the particles come
 764 from boulders with thermal inertia of $200 \text{ J m}^{-2} \text{ K}^{-1} \text{ s}^{-1/2}$. One could also use a plot like this to
 765 estimate regolith particle thermal conductivity, with enough information. For example, if the
 766 effective particle size is known to be less than 1.8 cm , we could conclude that the particles
 767 cannot be made of the low thermal inertia boulder material.

768 A recent study by Cambioni et al. (2021) presents evidence that the high thermal inertia
 769 boulders on Bennu and other primitive bodies are more likely to produce regolith particles than
 770 the low thermal inertia boulders due to different relative rates of fragmentation in response to
 771 meteoroid impacts and thermal fracturing. If the regolith particles at the Nightingale Site are
 772 indeed sourced predominantly from high thermal inertia boulders, then the effective particle size
 773 for this thermal inertia value would be $\sim 1\text{--}1.5 \text{ cm}$ in diameter, which is consistent with
 774 observations of abundant resolved and unresolved particles $< 2 \text{ cm}$ (Burke et al., 2021; Walsh et
 775 al., *in revision*). However, the thermal inertia estimates for the Nightingale site still include
 776 contributions of rocks and fine regolith (Rozitis et al., 2020). Thus, we await thermal modeling
 777 results using the highest spatial resolution data from the TAG operation that might cover areas
 778 with only particles smaller than the diurnal skin depth before attempting a robust quantitative
 779 analysis of the thermophysical properties of the returned sample.

780

781 **6 Conclusions and Future Work**

782 We have numerically determined the effective radiative thermal conductivity and
 783 radiative exchange factor of random and regular packings of spheres in order to investigate the
 784 effects of porosity and particle thermal conductivity on the observed thermal inertia of airless
 785 body regolith. Our results are in agreement with experimental data from Sakatani et al. (2017;
 786 2018) and show a new relationship between regolith radiative thermal conductivity, porosity, and
 787 the particle non-isothermality that was not predicted across the full range of porosity ($\sim 0.35\text{--}0.8$)
 788 by any other models. We have also found that regular packings have a radiative exchange factor
 789 that is $10\text{--}25\%$ lower than random packings in the range of porosities where both were examined
 790 ($\sim 0.45\text{--}0.80$). As such, future investigators should not use regular packings as an approximation
 791 for random packings in studies of radiative heat transfer, despite their relative numerical and
 792 analytical convenience.

793 The resulting expression for the radiative thermal conductivity of regolith is represented
 794 in Equation 8, making use of our new expression and coefficients for the radiative exchange

795 factor, F (Equation 8, $a=0.739$, $b=0.629$, and $c=1.031$), and the non-isothermality effect, f_k
 796 (Equation 12, $a_1=-0.500$, $a_2=1.351$, $a_3=0.741$, and $a_4=1.007$).

797 There are several outstanding questions in the study of regolith thermal properties and the
 798 interpretation of thermal inertia results. We note a few high-priority items here that should be
 799 addressed in future studies:

- 800 • The effects of non-unitary emissivity on regolith bulk radiative conductivity should be
 801 incorporated into our porosity-dependent expressions for F and f_k . Our model does not
 802 currently support non-unitary emissivity, but it is in development.
- 803 • The apparent particle-size dependence of experimental fit parameters ζ and ξ (Sakatani et
 804 al., 2017; 2018) has yet to be conclusively explained. It is likely that more experimental
 805 data are needed to determine if this is a real phenomenon.
- 806 • The bulk radiative thermal conductivity of polydisperse particulates was shown to be
 807 represented by the Sauter mean particle diameter in our previous study (Ryan et al.,
 808 2020). However, we are concerned that the particle size ranges used in that work were
 809 too narrow to conclusively distinguish between the Sauter mean and the volumetric
 810 median (c.f., Sakatani et al., 2018) as the representative particle diameter. Furthermore,
 811 the solid conduction term may have a different representative particle size, given that the
 812 governing equations for heat flow through particle contacts differ significantly from those
 813 that describe radiative conduction. Detailed experimentation or very large numerical
 814 models will be required to capture the necessarily large representative volume elements
 815 with wide ranges of particle sizes. Numerical investigations might be better suited to a
 816 less-intensive discrete element method model where all particles are modeled as having
 817 an internally uniform temperature, but this would be at the cost of losing information on
 818 the non-isothermality effect.
- 819 • The bulk solid conduction of a particle assemblage is controlled by the details of the
 820 particle-to-particle contacts, which are affected by assemblage packing density and many
 821 properties of the individual particles, including shape, roughness, and surface energy
 822 (related to composition and surface cleanliness). Much progress has been made on this
 823 subject in recent years (e.g., Sakatani et al., 2018; Arakawa et al., 2019; Wood, 2020;
 824 Arakawa, 2020), but there are still uncertainties in how these effects might scale with
 825 particle size.
- 826 • The apparent thermal inertia of a surface will transition from being controlled by the
 827 properties of a particulate assemblage to the properties of a single particle (a.k.a. boulder)
 828 as the particle size exceeds the diurnal skin depth. The details of this transition are not
 829 known in detail, aside from the assumption that it will occur when the particle size
 830 approximately exceeds the diurnal skin depth. We intend to address this in our next
 831 manuscript.
- 832 • Finally, as mentioned in our discussion, it is unclear what temperature to use when
 833 interpreting model-derived thermal inertia values in terms of regolith particle size. Given
 834 the strongly temperature-dependent thermal conductivity of coarse regolith, the
 835 instantaneous thermal inertia will change throughout the diurnal cycle. However, we
 836 expect that the overall diurnal profile can be approximated with the thermal properties of
 837 the regolith at or near the mean diurnal temperature. This expectation should be verified
 838 under a range of conditions, including different regolith material properties, rotation
 839 periods, and heliocentric distances.

840 **Acknowledgments and Data Availability**

841 This work was primarily funded by NASA Solar System Workings Grant 80NSSC21K0146. The
 842 authors acknowledge support from the Academies of Excellence on Complex Systems and
 843 Space, Environment, Risk and Resilience of the Initiative d'EXcellence (IDEX) Joint, Excellent,
 844 and Dynamic Initiative (JEDI) of the Université Côte d'Azur as well as from the Centre National
 845 d'Études Spatiales (CNES). B.R. acknowledges funding support from the UK Science and
 846 Technology Facilities Council (STFC). This material is based in part upon work supported by
 847 NASA under Contract NNM10AA11C issued through the New Frontiers Program. We thank
 848 Ron Ballouz for sharing his code for generating sphere packings using the method by Ringl et al.
 849 (2012). We also thank Mark Bentley for making his aggregate packing code publicly available
 850 on his GitHub page (<https://github.com/msbentley/aggregate>). The portion of the aggregate code
 851 that we modified to include periodicity is available in an external archive, along with our model
 852 geometry/solution files, script for processing model outputs, and a summary calculation
 853 spreadsheet (Ryan, 2022; <https://doi.org/10.5281/zenodo.5839026>). The authors declare no real
 854 or perceived conflicts of interest.

855

856 **References**

- 857 Arakawa, S., Tanaka, H., Katoaka, A., & Nakamoto, T. (2017). Thermal conductivity of porous
 858 aggregates. *Astronomy and Astrophysics*, *608*, L7. doi:10.1051/0004-6361/201732182
- 859 Arakawa, S., Tatsuuma, M., Sakatani, N., & Nakamoto, T. (2019). Thermal conductivity and
 860 coordination number of compressed dust aggregates. *Icarus*, *324*, 8–14.
 861 doi:10.1016/j.icarus.2019.01.022
- 862 Arakawa, S. (2020) Revisiting sticking property of submillimetre-sized aggregates. *Monthly
 863 Notices of the Royal Astronomical Society*, *496*, 2786–2789. doi:10.1093/mnras/staa1764
- 864 Ballouz, R.-L., Walsh, K. J., Sánchez, P., Holsapple, K.A., Michel, P. Scheeres, D. J., et al.,
 865 (2021). Modified granular impact force laws for the OSIRIS-REx touchdown on the surface
 866 of asteroid (101955) Bennu. *Monthly Notices of the Royal Astronomical Society*, *507*, 5087–
 867 5105. doi:10.1093/mnras/stab2365
- 868 Bandfield, J.L., Ghent, R.R., Vasavada, A.R., Paige, D.A., Lawrence, S.J., & Robinson, M.S.
 869 (2011) Lunar surface rock abundance and regolith fines temperatures derived from LRO
 870 Diviner Radiometer data. *Journal of Geophysical Research*, *116*, E00H02.
 871 doi:10.1029/2011JE003866
- 872 Birch, F. & Clark, H. (1940) The thermal conductivity of rocks and its dependence upon
 873 temperature and composition. *American Journal of Science*, *238*(8), 529–558.
- 874 Birch, F. & Law, R. R. (1935) Measurement of compressibility at high pressures and high
 875 temperatures. *Bulletin of the Geological Society of America*, *46*, 1219–1250.
- 876 Breitbach, G., & Barthels, H. (1980) The radiance heat transfer in the high temperature reactor
 877 core after failure of the afterheat removal systems. *Nuclear Technology*, *49*(3), 392–399.
 878 doi:10.13182/NT80-A17687

- 879 Burke, K. N., DellaGiustina, D. N., Bennett, C. A., Walsh, K. J., Pajola, M., Bierhaus, E. B., et
 880 al., (2021) Particle Size-Frequency Distributions of the OSIRIS-REx Candidate Sample Sites
 881 on Asteroid (101955) Bennu. *Remote Sensing*, *13*, 1315. doi:10.3390/rs13071315
- 882 Calderón-Vásquez, I., Cortés, E., García, J., Segovia, V., Caroca, A., Sarmiento, C., et al. (2021)
 883 Review on modeling approaches for packed-bed thermal storage systems. *Renewable and*
 884 *Sustainable Energy Reviews*, *143*, 110902. doi:10.1016/j.rser.2021.110902
- 885 Cambioni, S., Delbo, M., Ryan, A. J., Furfaro, R., & Asphaug, E. (2019). Constraining the
 886 thermal properties of planetary surfaces using machine learning: Application to airless
 887 bodies. *Icarus*, *325*, 16–30. doi:10.1016/j.icarus.2019.01.017
- 888 Cambioni, S., Delbo, M., Poggiali, G., Avdellidou, C., Ryan, A. J., et al. (2021) Fine-regolith
 889 production on asteroids controlled by rock porosity, *Nature*, *598*, 49–52.
- 890 Choudhary, M. K. & Potter, R. M. (2005) Heat Transfer in Glass-Forming Melts, in Properties of
 891 *Glass-Formation Melts*, edited by D. L. Pye, A. Montenaro, I. Joseph; CRC Press, Boca
 892 Raton.
- 893 Christensen, P. R., J. L. Bandfield, V. E. Hamilton, D. A. Howard, M. D. Lane, J. L. Piatek, S.
 894 W. Ruff, & W. L. Stefanov (2000b), A thermal emission spectral library of rock-forming
 895 minerals, *J. Geophys. Res.*, *105*(E4), 9735–9739.
- 896 De Beer, M., Rousseau, P. G., & du Toit, C. G. (2018). A review of methods to predict the
 897 effective thermal conductivity of packed pebble beds, with emphasis on the near-wall region.
 898 *Nuclear Engineering and Design*, *331*, 248–262. doi:10.1016/j.nucengdes.2018.02.029
- 899 Delbo, M., M. Mueller, J. P. Emery, B. Rozitis, & M. T. Capria (2015), Asteroid thermophysical
 900 modeling, in *Asteroids IV*, edited by P. Michel, F. DeMeo, & W. F. Bottke, pp. 107–128, The
 901 University of Arizona Press, Tucson.
- 902 Emery, J. P., Fernández, Y. R., Kelley, M. S. P., nève Crane, K. T. W., Hergenrother, C., Lauretta,
 903 D. S., et al. (2014). Thermal infrared observations and thermophysical characterization of
 904 OSIRIS-REx target asteroid (101955) Bennu. *Icarus*, *234*(C), 17–35.
 905 doi:10.1016/j.icarus.2014.02.005
- 906 Ferguson, R. L., P. R. Christensen, J. F. Bell III, M. P. Golombek, K. E. Herkenhoff, & Kieffer,
 907 H. H. (2006), Physical properties of the Mars Exploration Rover landing sites as inferred
 908 from Mini-TES–derived thermal inertia, *Journal of Geophysical Research*, *111*(E2), E02S21.
 909 doi:10.1029/2005JE002583
- 910 Flynn, G. J., Consolmagno, G. J., Brown, P., & Macke, R. J. (2018). Physical properties of the
 911 stone meteorites: Implications for the properties of their parent bodies. *Chemie de Erde*, *78*,
 912 269–298. doi:10.1016/j.chemer.2017.04.002
- 913 Garboczi, E. J. (2011) Three dimensional shape analysis of JSC-1A simulated lunar regolith
 914 particles. *Powder Technology*, *207*, 96–103. doi:10.1016/j.powtec.2010.10.014
- 915 Grott, M., Knollenberg, J., Hamm, M., Ogawa, K., Jaumann, R., Otto, K., et al. (2019). Low
 916 thermal conductivity boulder with high porosity identified on C-type asteroid (162173)
 917 Ryugu. *Nature Astronomy*, *3*, 971–976. doi:10.1038/s41550-019-0832-x

- 918 Gundlach, B., & Blum, J. (2012). Outgassing of icy bodies in the Solar System – II: Heat
 919 transport in dry, porous surface dust layers. *Icarus*, 219(2), 618–629.
 920 doi:10.1016/j.icarus.2012.03.013
- 921 Gundlach, B., & Blum, J. (2013). A new method to determine the grain size of planetary
 922 regolith. *Icarus*, 223(1), 479–492. doi:10.1016/j.icarus.2012.11.039
- 923 Henderson, B. G. & Jakosky, B. M. (1994) Near-surface thermal gradients and their effects on
 924 mid-infrared emission spectra of planetary surfaces. *Journal of Geophysical Research*,
 925 99(E9), 19063–19073.
- 926 Hitti, K., & Bernacki, M. (2013). Optimized Dropping and Rolling (ODR) method for packing of
 927 poly-disperse spheres. *Applied Mathematical Modelling*, 37(8), 5715–5722,
 928 doi:10.1016/j.apm.2012.11.018
- 929 Jakob, M. (1949), *Heat Transfer*, 1st ed., John Wiley & Sons, New York.
- 930 Kaviany, M. (1995), *Principles of Heat Transfer in Porous Media*, 2nd ed., Springer, New York.
- 931 Licandro, J., Müller, T., Alvarez, C., Alí-Lagoa, V., & Delbo, M. (2016) GTC/CanariCam
 932 observations of (99942) Apophis. *Astronomy & Astrophysics*, 585, A10. doi: 10.1051/0004-
 933 6361/201526888
- 934 McKay, D. S., Carter, J. L., Boles, W. W., Carlton, C. A., & Allton, J. H. (1994) JSC-1: A new
 935 lunar soil stimulant. *Proc., Symp. 94*, ASCE, New York, 857–866.
- 936 Merrill, R. B. (1969). Thermal conduction through an evacuated idealized powder over the
 937 temperature range of 100 to 500 K, *NASA Technical Note D-5063*.
 938 <https://ntrs.nasa.gov/search.jsp?R=19690010650>.
- 939 Murdoch, N., Sánchez, P., Schwartz, S. R., & Miyamoto, H. (2015) Asteroid Surface
 940 Geophysics, in *Asteroids IV*, edited by P. Michel, F. DeMeo, & W. F. Bottke, pp. 767–793,
 941 The University of Arizona Press, Tucson.
- 942 Nakamura, T., Noguchi, T., Tanaka, M., Zolensky, M.E., Kimura, M., Tsuchiyama, A., et al.
 943 (2011). Itokawa Dust Particles: A Direct Link Between S-Type Asteroids and Ordinary
 944 Chondrites. *Science*, 333(6046), 1113–1116. doi: 10.1126/science.1207758
- 945 Okada, T., Yamamoto, Y., Inoue, T., Shirai, K., Arai, T., Ogawa, K., et al. (2006). Thermal
 946 radiometry of asteroid Itokawa by the XRS onboard Hayabusa. *Lunar and Planetary Science*
 947 XXXVII, Abstract 1965.
- 948 Opeil, C. P., Britt, D. T., Macke, R. J., & Consolmagno, G. J. (2020) The surprising thermal
 949 properties of CM carbonaceous chondrites. *Meteoritics & Planetary Science*. doi:
 950 10.1111/maps.13556
- 951 Presley, M. A., & Christensen, P. R. (1997). Thermal conductivity measurements of particulate
 952 materials: 1. A review. *Journal of Geophysical Research*, 102(E3), 6535–6549.
 953 doi:10.1029/96JE03302
- 954 Ringl, C., Bringa, E. M., Bertoldi, D. S., & Urbassek, H. M. (2012) collisions of porous clusters:
 955 A granular-mechanics study of compaction and fragmentation. *The Astrophysical Journal*,
 956 752(151). doi:10.1088/0004-637X/752/2/151

- 957 Robertson, E. C., & Peck, D. L. (1974), Thermal Conductivity of Vesicular Basalt from Hawaii.
 958 *Journal of Geophysical Research*, 79(32), 4875–4888.
- 959 Robold, K. (1982), *Wärmetransport im inneren und in der Randzone von Kugeischüttungen*,
 960 Dissertation Jul-1796, Nuclear Research Center, Jülich.
- 961 Rozitis B., Ryan, A. J., Emery, J. P., Christensen, P. R., Hamilton, V. E., Simon, A. A., et al.
 962 (2020) Thermal Inertia Maps of (101955) Bennu from OSIRIS-REx Infrared Observations.
 963 *Science Advances*, 6, eabc3699. doi: 10.1126/sciadv.abc3699
- 964 Rozitis, B. & Green, S. F. (2011) Directional characteristics of thermal–infrared beaming from
 965 atmosphereless planetary surfaces – a new thermophysical model. *Monthly Notices of the*
 966 *Royal Astronomical Society*, 415, 2042–2062.
- 967 Ryan, A. J. (2022). Data and scripts for manuscript "Full-field modeling of heat transfer in
 968 asteroid regolith 2: Effects of porosity" [Data set]. Zenodo. doi:10.5281/zenodo.5839026
- 969 Ryan, A. J., Pino Muñoz, D., Bernacki, M., & Delbo, M. (2020) Full-Field Modeling of Heat
 970 Transfer in Asteroid Regolith: Radiative Thermal Conductivity of Polydisperse Particulates.
 971 *Journal of Geophysical Research: Planets*, 125, e2019JE006100. doi:10.1029/2019JE006100
- 972 Sakatani, N., Ogawa, K., Arakawa, M., & Tanaka, S. (2018). Thermal conductivity of lunar
 973 regolith simulant JSC-1A under vacuum. *Icarus*, 309, 13–24.
 974 doi:10.1016/j.icarus.2018.02.027
- 975 Sakatani, N., Ogawa, K., Iijima, Y., Arakawa, M., Honda, R., & Tanaka, S. (2017). Thermal
 976 conductivity model for powdered materials under vacuum based on experimental studies.
 977 *AIP Advances*, 7(1), 015310–24. doi:10.1063/1.4975153
- 978 Salisbury, J. W. & D’Aria, D. M. (1992) Emissivity of terrestrial materials in the 8–14
 979 micrometer atmospheric window. *Remote Sensing of Environment*, 42, 83–106.
- 980 Schotte, W. (1960). Thermal conductivity of packed beds. *AIChE Journal*, 6(1), 63–67.
 981 doi:10.1002/aic.690060113.
- 982 Shimaki, Y., Senshu, H., Sakatani, N., Okada, T., Fukuhara, T., Tanaka, S., et al. (2020)
 983 Thermophysical properties of the surface of asteroid 162173 Ryugu: Infrared observations
 984 and thermal inertia mapping. *Icarus*, 348, 113835. doi:10.1016/j.icarus.2020.113835
- 985 Sibille, L., Carpenter, P., Schlagheck, R., & French, R. A. (2006) Lunar Regolith Simulant
 986 Materials: Recommendations for Standardization, Production, and Usage. *NASA Technical*
 987 *Report 2006-214605*.
- 988 Singh, B. P., & Kaviany, M. (1994). Effect of solid conductivity on radiative heat transfer in
 989 packed beds. *International Journal of Heat and Mass Transfer*, 37(16), 2579–2583,
 990 doi:10.1016/0017-9310(94)90295-X
- 991 Skorov, Y., van Lieshout, R., Blum, J., & Keller, H. U. (2011) Activity of comets: Gas transport
 992 in the near-surface porous layers of a cometary nucleus. *Icarus*, 212, 867–876.
 993 doi:10.1016/j.icarus.2011.01.018
- 994 Sorli, K. C. & Hayne, P. O. (2020) Thermophysical modeling of 99942 Apophis: Estimations of
 995 surface temperature during the April 2029 close approach. *Apophis T–9 Years 2020*, LPI
 996 Contrib. No. 2242. Abstract 2069.

- 997 Tamari, S., Samaniego- Martínez, D., Bonola, I., Banbala, E. R., Ordaz-Chaparro, V. (2005)
 998 Particle Density of Volcanic Scoria Determined by Water Pycnometry. *Geotechnical Testing*
 999 *Journal*, 28(4), GTJ12675.
- 1000 Tausendschön, J. & Radl, S. (2021) Deep neural network-based heat radiation modelling
 1001 between particles and between walls and particles. *International Journal of Heat and Mass*
 1002 *Transfer*, 177, 121557. doi:10.1016/j.ijheatmasstransfer.2021.121557
- 1003 Taylor, L. A., Hill, E., Liu, Y., & Day, J. M. (2005). JSC-1 as the Lunar Soil Simulant of Choice.
 1004 *Meteoritics and Planetary Science Supplement*, 40, 5180.
- 1005 Touloukian, Y. S. & DeWitt, D. P. (1972) *Thermophysical Properties of Matter - The TPRC*
 1006 *Data Series. Volume 8. Thermal Radiative Properties - Nonmetallic Solids*.
- 1007 van Antwerpen, W., Rousseau, P. G., & du Toit, C. G. (2012). Multi-sphere Unit Cell model to
 1008 calculate the effective thermal conductivity in packed pebble beds of mono-sized spheres.
 1009 *Nuclear Engineering and Design*, 247, 183–201. doi:10.1016/j.nucengdes.2012.03.012
- 1010 van Antwerpen, W., du Toit, C. G., & Rousseau, P. G. (2010). A review of correlations to model
 1011 the packing structure and effective thermal conductivity of packed beds of mono-sized
 1012 spherical particles. *Nuclear Engineering and Design*, 240(7), 1803–1818.
 1013 doi:10.1016/j.nucengdes.2010.03.009
- 1014 Vortmeyer, D. (1979) Wärmestrahlung in dispersen Feststoffsystemen. *Chem. Ing. Tech.*, 51(9),
 1015 839–851.
- 1016 Wada, K., Grott, M., Michel, P., Walsh, K. J., Barucci, A. M., Biele, J., et al. (2018) Asteroid
 1017 Ryugu before the Hayabusa2 encounter. *Progress in Earth and Planetary Science*, 5(82).
 1018 doi:10.1186/s40645-018-0237-y
- 1019 Walsh, K. J., Bierhaus, E.B., Lauretta, D. S., Nolan, M.C., Ballouz, R.-L., Bennet, C. A., et al.
 1020 (in revision). Assessing the sampleability of Bennu’s surface for the OSIRIS-REx asteroid
 1021 sample return mission. *Space Science Reviews*.
- 1022 Watson, K. (1964). *The thermal conductivity measurements of selected silicate powders in*
 1023 *vacuum from 150 degrees-350 degrees K* (Doctoral dissertation). Pasadena, CA: California
 1024 Institute of Technology. <https://resolver.caltech.edu/CaltechETD:etd-11042002-153232>.
- 1025 Warren, T. J., Bowles, N. E., Donaldson Hanna, K., & Bandfield, J. L. (2019). Modeling the
 1026 angular dependence of emissivity of randomly rough surfaces. *Journal of Geophysical*
 1027 *Research: Planets*, 124, 585–601. doi:10.1029/2018JE005840
- 1028 Wechsler, A. E., Glaser, P. E., & Fountain, J. A. (1972). Thermal Properties of Granulated
 1029 Materials. In J. W. Lucas (Ed.), *Thermal Characteristics of the Moon*. Cambridge, MA: MIT
 1030 Press.
- 1031 Wesselink, A. J. (1948). Heat conductivity and nature of the lunar surface material. *Bulletin of*
 1032 *the Astronomical Institutes of the Netherlands*, 10(390), 351–363.
- 1033 Wood, S. E. (2020) A mechanistic model for the thermal conductivity of planetary regolith: 1.
 1034 The effects of particle shape, composition, cohesion, and compression at depth, *Icarus*, 352,
 1035 113964. doi:10.1016/j.icarus.2020.113964

- 1036 Woodside, W. & Messmer, J. H. (1961). Thermal conductivity in porous media II. Consolidated
 1037 rocks. *Journal of Applied Physics*, 32, 1699–1706. doi:10.1063/1.1728420
- 1038 Wu, H., Gui, H., Yang, X., Tu, J., & Jiang, S. (2020). A matrix model of particle-scale radiative
 1039 heat transfer in structured and randomly packed pebble bed. *International Journal of*
 1040 *Thermal Sciences*, 153, 106334.
- 1041 Zeng, X., He, C., Oravec, H., Wilkinson, A., Agui, J., & Asnani, V. (2010). Geotechnical
 1042 properties of JSC-1A lunar soil simulant. *Journal of Aerospace Engineering*, 23(2), 111–116.
 1043 doi:10.1061/(ASCE)AS.1943-5525.0000014
- 1044